Tuning oxygen vacancies and realizing self-compliance resistive switching in a WO_x memristor

Mengyao Chen(陈梦瑶)[1], Wenshuai Gao(高文帅)[1,†], and Hongjun Wang(王红军)[2,‡]

[1] *Information Materials and Intelligent Sensing Laboratory of Anhui Province, Center of Free Electron Laser & High Magnetic Field, Institutes of Physical Science and Information Technology, Anhui University, Hefei* 230601, *China*

[2] *School of Physics & Information Science, Shaanxi University of Science and Technology, Xi'an* 710021, *China*

(Received 10 September 2025; revised manuscript received 19 October 2025; accepted manuscript online 21 November 2025)

Tungsten oxide (WO_x) has attracted widespread attention as a new type of memory functional material with development and application prospects in industry. However, research into the effect of electrodes on the properties of WO_x-based switching memories remains insufficient. Here, non-crystalline WO_x-based switching memories were prepared with four electrodes (Ti, Al, TiN and W), and all the devices displayed nonvolatile resistive switching (RS) behavior. Notably, the W/WO_x/Pt structure of the memristor still has excellent performance without compliance current, including high retention characteristics, a wide ON/OFF window, ultra-low set/reset voltages and a fast response time. In addition, a physical model is given to further explain the electrode modulation of oxygen vacancy conducting filaments. This study provides a strategy for optimizing the electrodes to tune the carrier transport mechanism and RS behavior of WO_x-based devices, which offers ideas for realizing highly stable self-compliance in current digital storage.

Keywords: resistive random-access memory, self-compliance, tungsten oxide

PACS: 72.20.–i, 73.40.Rw, 61.72.jd, 68.60.–p

DOI: 10.1088/1674-1056/ae2264 **CSTR:** 32038.14.CPB.ae2264

CPB Online In-Press

1. Introduction

Recently, the demand for information storage has exploded with the vigorous development of artificial intelligence and the Internet of Things.[1–7] While NAND flash has achieved an excellent theoretical cell size of $4F^2$, its further scaling faces critical physical challenges. These include severe cell-to-cell interference and the degradation of charge retention at scaled dimensions, which hinder both storage density and reliability.[8,9] Consequently, alternative memory technologies are urgently needed to meet future storage requirements.[10] Emerging non-volatile memories have begun to be studied and some progress has been made in addressing the difficulty of shrinking the physical size of traditional charge storage devices, including ferroelectric random access memory (FeRAM),[11,12] magnetic random access memory (MRAM),[13,14] phase change memory (PCM)[15,16] and resistive random access memory (RRAM).[17–19] Among these, RRAM is considered to be a particularly promising candidate. This is not because its attributes are entirely unique but because it offers a compelling and balanced combination of a simple two-terminal structure, excellent scalability, low power consumption and superior complementary metal–oxide–semiconductor (CMOS) compatibility.[20] This combination positions RRAM favorably for next-generation high-density memory and neuromorphic computing applications.[21–24]

The stability, multi-level storage characteristics and fast response characteristics of memory devices mainly depend on the stacking of materials, thus the selection of materials for the switching layer is particularly significant. There is a wide choice of materials for switching layers, and almost all insulator and semiconductor materials can be used for memories.[25,26] Therefore, some materials with potential resistive switching properties are highly valued, such as binary metal oxides, complex metal oxides, inorganic and organic compounds and other new thin film materials.[27–29] Binary metal oxides (WO_x, VO_x, TaO_x, TiO_x, HfO_x, etc.) are favored by industry due to the advantages of ease of preparation, controllable composition, stable performance and low cost.[30–34] While tungsten oxide (WO_x) is a well-established material in this field, it continues to be the subject of extensive investigation. This enduring interest is driven by its attractive properties, such as high thermal stability, a relatively narrow band gap (2.4–3.2 eV) and highly tunable resistive switching characteristics.[35–37] Moreover, there are a large number of oxygen vacancy defects in amorphous WO_x, which has great potential for application in resistive switching devices based on oxygen vacancy migration.[38]

One characteristic that exists with RRAMs is that the compliance current is typically applied during formation to avoid hard breakdown. The absence of a compliance current may cause the device to be irreversibly damaged and remain in

†Corresponding author. E-mail: gwsh@ahu.edu.cn

‡Corresponding author. E-mail: wanghongjun@sust.edu.cn

© 2026 Chinese Physical Society and IOP Publishing Ltd. All rights, including for text and data mining, AI training, and similar technologies, are reserved.

a low resistance state (LRS) forever.[39–41] Nevertheless, previous studies have revealed that specific device architectures or intrinsic physical mechanisms are capable of inherently limiting the current, thereby eliminating the need for external compliance circuitry, which is called the self-compliance property. Therefore, investigations of self-compliance devices will broaden the applications of RRAM.[42] Furthermore, it is well understood that the selection of electrodes has a significant impact on the performance of memory devices.[43] The choice of top electrode (TE) can seriously affect the competition and trapping of oxygen vacancies that occur at the interface with the switching layer, which is critical for the formation and rupture of conducting filaments (CFs). Therefore, it is crucial to investigate the interface effects between the TE and the switching layer to enhance memory performance and achieve self-compliance by understanding the regulation of oxygen vacancies through different electrodes.

In this work, metal and ceramic materials with different work functions are selected as the TE to construct the memory, while stable Pt and amorphous WO_x films are used as the bottom electrode (BE) and switching layer, respectively. Experimental results show that all devices exhibit significant bipolar RS behavior, and importantly, modulation of oxygen vacancy migration enables self-compliance effects. Moreover, the W/WO_x/Pt devices have superior switching performance, including ultra-low set/reset voltages and high retention characteristics.

2. Experimental details

In this work, Si was selected as the substrate to construct the device. It was cleaned with acetone, alcohol and deionized water for 10 min in sequence. Then, a Pt metal layer with a thickness of about 100 nm was deposited on the Si substrate as the BE by using the DC magnetron sputtering method. The WO_x layer was deposited on the Pt/Si substrate by radio frequency magnetron sputtering. Tungsten metal with a thickness of 5 mm, a radius of 30 mm and a purity of 99.95% was selected as the sputtering target. The degree of vacuum in the target chamber was initially lower than 8×10^{-4} Pa, the ignition pressure was set to 5 Pa, and the working pressure during sputtering was maintained at 2 Pa with 100 W sputtering power. The flow rates of Ar and O_2 were 30 sccm and 10 sccm, respectively, and the deposition time was 10 min under 250 °C. Finally, with a mask diameter of 30 μm, Ti, Al, TiN and W were deposited on the WO_x film as the TE to create memory devices (Ti/WO_x/Pt, Al/WO_x/Pt, TiN/WO_x/Pt and W/WO_x/Pt).

The current–voltage (I–V) characteristics of the devices were measured at room temperature using an Agilent B1500A semiconductor parameter analyzer. To conduct the measurement, a DC bias voltage was applied to the TE while the BE was grounded. Additionally, a positive compliance current (I_{CC}) was set during the I–V measurement to prevent the device from completely breaking down.

X-ray diffraction (XRD; Bruker D8 Advanced) and x-ray photoelectron spectroscopy (XPS; ESCALAB 250Xi) were utilized to analyze the crystal structure, crystallinity, and chemical bond distribution of the WO_x films. The surface and cross-sectional morphology of the device were assessed using a scanning electron microscope (SEM; FEI Quanta 200 F) to verify the density and thickness of the prepared switching layer.

3. Results and discussion

The TE/WO_x/Pt device structure is illustrated in Fig. 1(a). To determine the crystalline phase of the WO_x films, XRD was performed at room temperature, as shown in Fig. 1(b). The absence of distinct diffraction peaks indicates that the WO_x films are amorphous. To further explore the microscopic morphology of the switching layer, the surface and cross-section of the WO_x film were characterized by SEM measurements, as depicted in Figs. 1(c) and 1(d). The surface of the film is relatively dense and homogeneous without any apparent pinholes. The cross-sectional thickness is uniform, with a switching layer thickness of 27.9 nm. Furthermore, the film was determined to be WO_x through energy-dispersive x-ray (EDS) spectroscopic scanning (the EDS spectrum is shown in Fig. S1 in the supplementary material).

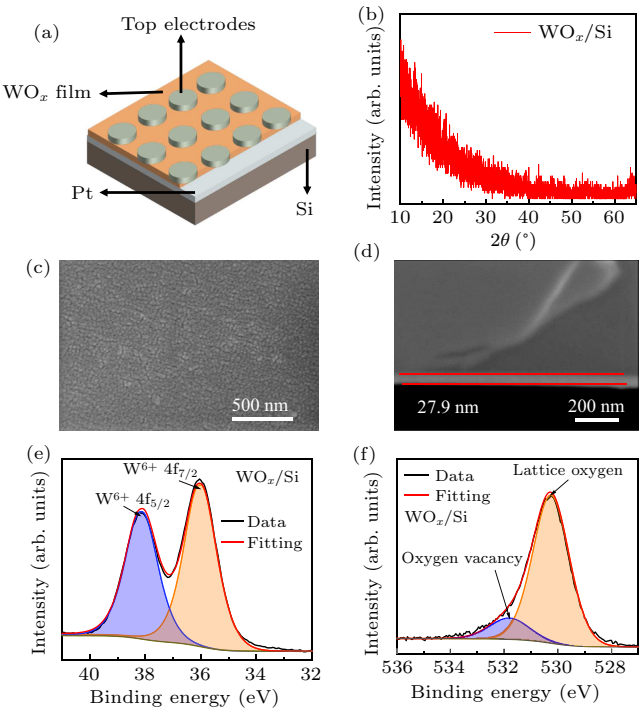


Fig. 1. (a) Schematic illustration of a WO_x-based memory device. (b) Typical XRD pattern of WO_x films. (c) Top-view SEM image of WO_x film. (d) Cross-sectional SEM image of WO_x film. XPS spectra of (e) W 4f and (f) O 1s in WO_x film.

CPB Online In-Press

To determine the elemental composition and chemical valence of the switching layer, the WO_x films were analyzed by XPS, as depicted in Figs. 1(e) and 1(f). The W 4f spectrum displays two spin–orbit states with binding energies of 38.15 eV and 36 eV assigned to W $4f_{5/2}$ and W $4f_{7/2}$, respectively. The O spectra show two bands at 531.7 eV and 530.65 eV, which are attributed to oxygen vacancies and lattice oxygens, respectively.[44,45] This suggests that the switching layer is still predominantly composed of WO_3 and contains natural oxygen vacancies.

The mechanisms and interfacial effects influencing the RS behavior of WO_x-based memories were investigated by measuring the *I*–*V* cycling characteristics of devices with various electrode configurations (Al, Ti, TiN and W)/WO_x/Pt, as shown in Fig. 2. The *I*–*V* cycling characteristics of the devices were tested over approximately 200 cycles with an I_{CC} of 10 mA, and the longitudinal axis was expressed using the natural logarithm to facilitate clearer observation. The devices were switched from the high resistance state (HRS) to the LRS at a positive bias voltage, referred to as the set process. Subsequently, the devices were switched from the LRS to the HRS at an appropriate negative bias voltage. All devices exhibit the typical bipolar RS behavior between the LRS and HRS. By comparison, it can be seen that as the work function of the top electrode material increases, the ON/OFF ratio of the TE/WO_x/Pt device also increases. Notably, the W/WO_x/Pt device demonstrates self-compliance behavior, making it valuable for practical applications. The self-compliance behavior supports the unique switching mechanism of WO_x, which can be attributed to the thermodynamics of oxygen vacancy migration and local stoichiometric variation, resulting in weak and self-compliant CFs. Such an intrinsic mechanism suppresses overcurrent-induced breakdown, thereby improving endurance and operational robustness.

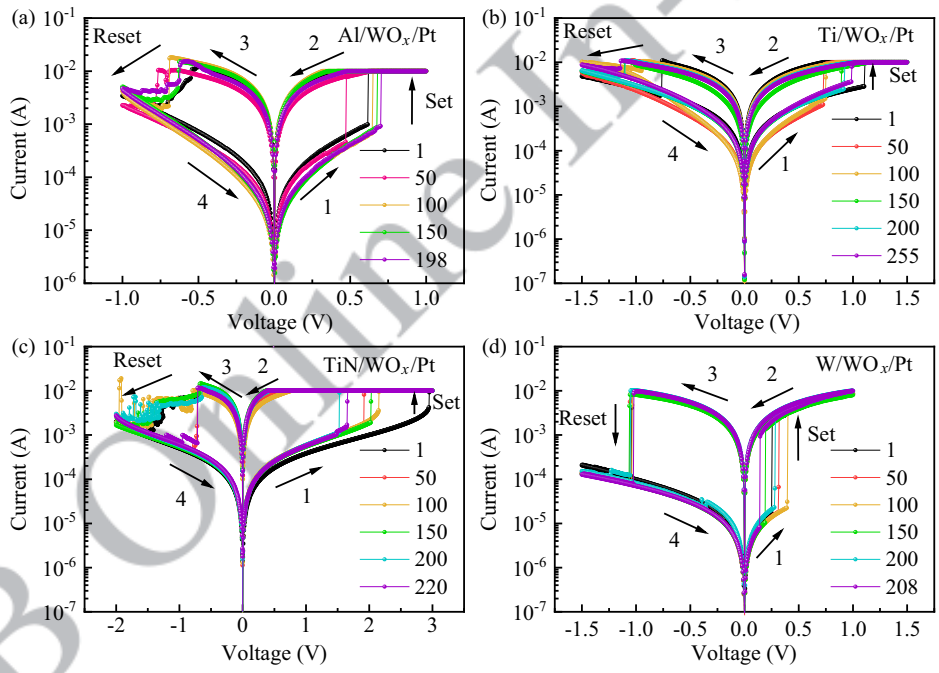


Fig. 2. Typical resistive switching *I*–*V* characteristics of TE/WO_x/Pt memristors with different top electrodes: (a) Al, (b)Ti, (c) TiN, (d) W.

The RS characteristics of the W/WO_x/Pt memristor are depicted in Fig. 3(a). Various I_{CC} values (0.1 mA, 1 mA, 5 mA and 10 mA) were applied during the set process to evaluate the *I*–*V* characteristics and investigate the device's multivalue storage capability. Because no oxide layer is formed at the W/WO_x interface, the resistance values of the HRS and LRS remain unaffected by the change of I_{CC}. In addition, the set voltage of the W/WO_x/Pt device gradually decreases with increasing I_{CC}, which is characteristic of the filamentary RS behavior.[46] However, when Ti and Al are used as the TE, an oxygen storage layer is formed at the TE/WO_x interfaces, increasing the number of oxygen vacancies. This makes the HRS decrease when I_{CC} is increased, which gives it the ability to store multiple values, as indicated in Fig. S2. Unlike many oxide-based memristors that exhibit analog or multilevel resistive switching, enabling gradual conductance modulation for synaptic weight tuning, the present WO_x-based device shows a distinct digital switching behavior even under different compliance current conditions (Fig. 3(a)). This feature originates from both the intrinsic material properties of WO_x and the simplicity of the device configuration.

Further, the distributions of set voltage (V_{set}) and reset voltage (V_{reset}) were obtained to examine the operational uniformity, as shown in Fig. 3(b). Remarkably, after more than 200 cycles of V_{set} and V_{reset} operations, the average values for the W/WO_x/Pt devices are 0.335 V and −1.051 V, respec-

CPB Online-Press

tively, exhibiting the more concentrated V_{reset} and lower V_{set}. The device exhibits relatively small and concentrated switching voltages, which is favorable for data storage applications. Moreover, a remarkably low power consumption (~ 3 μW) is achieved, as evidenced by the low set/reset voltages and the current levels in both resistance states. As depicted in Fig. S3, the TE/WO_x interface provides additional oxygen ions, which bind with the oxygen vacancies during the reset process. When TEs such as Al, Ti and TiN are employed, the instability of the RS behavior is caused by the occurrence of variations in the concentration of oxygen vacancies, so different configurations of TE lead to apparent alterations in the threshold voltage distribution. Moreover, Fig. 3(c) displays the forming voltage statistics for different devices. The forming voltage is still influenced by the material selected for the TE. The device with Ti exhibits the lowest forming voltage, while the device with W demonstrates the highest forming voltage. According to current theoretical calculations, the higher the vacancy formation energy of the electrode, the higher the voltage needed to form CFs.[47] When electrode materials with a lower vacancy formation energy (e.g., Al, Ti) form vacancy CFs, the oxygen vacancies are more uniformly distributed, and thus the forming voltage is lower and the distribution is more concentrated. For electrodes with high vacancy formation energies (e.g., TiN, W), the increase in the electric field leads to an increase in the internal temperature of the switching layer and the CFs will expand transversely. As a result, these devices exhibit a larger formation voltage and a less centralized distribution.

Figure 3(d) illustrates that the devices were tested between the HRS and LRS through approximately 200 transitions at a reading voltage of 0.05 V and an I_{CC} of 10 mA. The W/WO_x/Pt device exhibits not only a relatively stable but also a switching ratio that is two orders of magnitude higher than that of other devices. As shown in Fig. S4, when Al and Ti are the TE, the devices show apparent instability. However, the TiN/WO_x/Pt device shows good endurance performance, with small fluctuations in the HRS and LRS over 200 cycles and, overall, no noticeable evolution in the generals. Figure 3(e) presents the data retention characteristics of the W/WO_x/Pt device, tested over 10^4 s at a reading voltage of 0.05 V. The result demonstrates that the device has higher stability and a larger storage window. The features of other devices are depicted in Fig. S5. The HRS of the Al/WO_x/Pt and TiN/WO_x/Pt devices experiences a slight fluctuation around 10^4 s but maintains an overall stable performance, while the Ti/WO_x/Pt device shows instability. It can be hypothesized that this instability is due to the more unstable TiO_2 oxygen storage layer formed at the interface.

To further explore the read and erase capability of WO_x-based memory under transient conditions, the performance of the device was tested under fast pulses, as shown in Fig. 3(f) and Fig. S6, with a read voltage of 0.05 V and a pulse interval of 2 ms. Using the W/WO_x/Pt device as an example, the set/reset response times are ~ 70 μs, demonstrating utility in the field of data storage. It should be noted, however, that this value represents the measurement limit of our laboratory equipment. As evident from Fig. 3(f), the current response (red line) occurs within an extremely short duration after the pulse voltage (black line) is applied, and the response speed is significantly faster than those of the other three devices. In addition, the continuous cycle pulse behavior of the device was also tested with a reading of 0.05 V and a pulse interval of 20 ms (see Fig. S7 in the supplementary material). The results demonstrate the robustness as well as the reliability of the devices under continuous pulses.

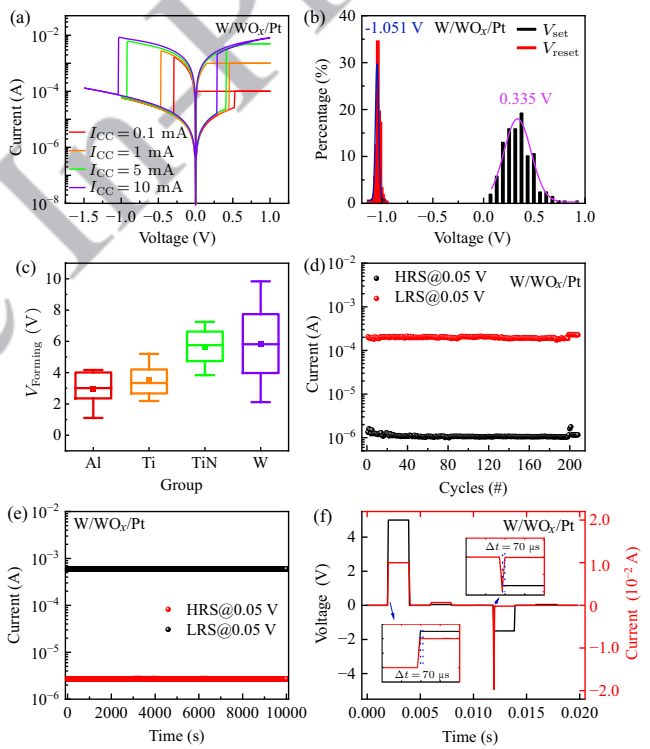


Fig. 3. *I*–*V* characteristics of W/WO_x/Pt memristors. (a) *I*–*V* characteristics under different I_{CC} values. (b) Statistical distribution of V_{set}/V_{reset}. (c) Forming voltage statistics. (d) Endurance performance at a reading voltage of 0.05 V. (e) Data retention characteristics at a reading voltage of 0.05 V. (f) Response speed measured for set/reset processes.

The investigation of the carrier transport mechanism of the device is a central basis for understanding and designing various memory devices. Here, we analyzed the double-log fitting analysis of the *I*–*V* curves. The results of the fitting in the positive scan region of the Al/WO_x/Pt device and the Ti/WO_x/Pt device are shown in Figs. 4(a) and 4(b). The fitting results for the HRS region can be divided into two parts: the low-voltage and high-voltage regions. The low-voltage region exhibits ohmic conduction behavior, while further detailed fitting was performed for the high-voltage region, specifically, where the current *I* is linearly related to the square of the voltage V^2. The results illustrate that both sets of devices are

CPB Online In Press

consistent with the theory of space-charge-limited conduction associated with traps.[48] Unlike the active metals discussed above, TiN and W exhibit distinct behaviors, with the corresponding I–V curves depicted in Figs. 4(c) and 4(d). When the devices are in the HRS, the fitting results are still divided into low- and high-voltage regions, and the low-voltage region still obeys the ohmic conduction theorem. However, in the high-voltage region, $\ln(I/V)$ is linearly related to $V^{1/2}$, unlike in the above, which is consistent with the Poole–Frenkel mechanism.[49,50] Furthermore, the LRS region of all devices exhibits a linear fit with a slope of approximately 1. The conduction mechanisms of the devices are all indicative of ohmic conduction, which is attributed to the formation of CFs.[51]

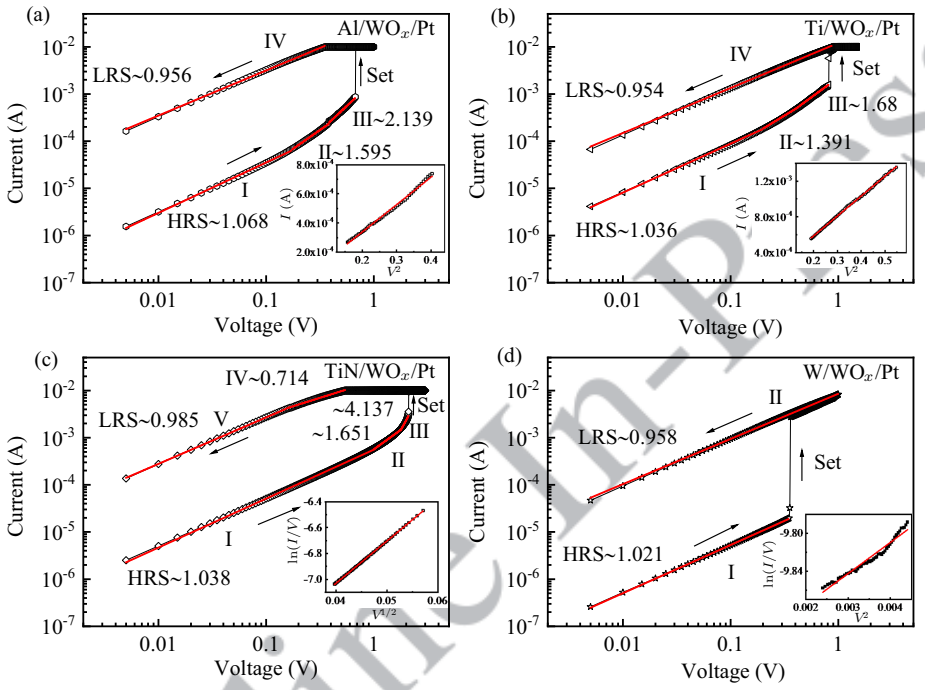


Fig. 4. Double-log fitting results for I–V curves in the positive sweep region of (a) Al/WO$_x$/Pt device, (b) Ti/WO$_x$/Pt device, (c) TiN/WO$_x$/Pt device and (d) W/WO$_x$/Pt device. Insets: fitted conductive mechanism of devices in a high electric field under the positive sweep region for the HRS.

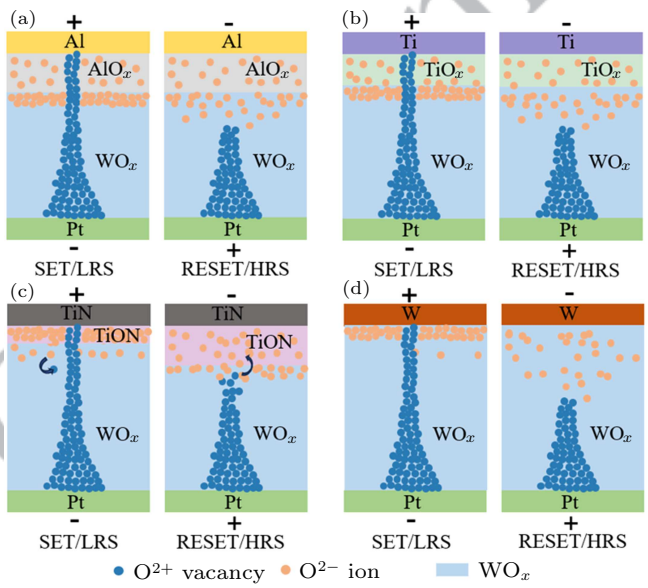


Fig. 5. Schematic diagrams of RS models for TE/WO$_x$/Pt memories: (a) Al/WO$_x$/Pt device, (b) Ti/WO$_x$/Pt device, (c) TiN/WO$_x$/Pt device, (d) W/WO$_x$/Pt device.

To further explain in detail the effect of the TE on the performance of WO$_x$-based memories, a simulation of the carrier transport inside the device is given in Fig. 5. The modulation of oxygen vacancies by the TE is consistent with a filamentary conduction mechanism, widely reported in inorganic oxide-based systems, and is evidenced by the characteristic inverse dependence of V_{set} on I_{CC}. When Al is the TE, the oxygen vacancies move toward the negative electrode and gradually accumulate, thereby forming oxygen-vacancy CFs connecting the TE and BE, enabling switching to the LRS during the set process. Meanwhile, oxygen ions move toward the TE, and AlO$_x$ is formed as the oxygen storage layer at the TE and WO$_x$. During the reset process, the oxygen ions move toward the BE to combine with the oxygen vacancies, which results in the rupture of CFs, and the device undergoes resistive state switching at this point. One thing to note is that the presence of an oxygen storage layer allows additional oxygen ions to encourage the rupture of CFs during the reset process. Moreover, the oxygen storage layer is equivalent to the series connection of the AlO$_x$ layer, so the value of the LRS resistance increases. The set and reset processes for Ti electrodes are similar to those for Al/WO$_x$/Pt devices. Compared with AlO$_x$, the stability of the TiO$_x$ is worse than that of the AlO$_x$, which further affects data retention. Nevertheless, an amorphous TiON layer is formed during the preparation of TiN. In the set process, the presence of additional oxygen ions in

the TiON layer restricts the movement of oxygen ions in the WO_x layer; consequently, a larger V_{set} is required to switch the resistive state. Conversely, the TiON oxygen storage layer makes the desired V_{reset} value small during the reset process. Finally, since W is an inert electrode, the migration of ions inside the switching layer during set and reset is irrelevant to the TE. Accordingly, the forming and rupture of the CFs of the W/WO_x/Pt device are more radical, and the pulse response time and storage window are faster and larger, respectively.

4. Conclusions

In summary, we carried out an optimization strategy to obtain stable high-performance TiO_x-based digital resistive memories by modulating the oxygen vacancies through modification of the electrodes (Al, Ti, TiN, and W). The results demonstrate that the W/WO_x/Pt device has a high storage window and a fast response time, indicating that the device has excellent self-compliance current data storage capability. The effect of electrodes on the performance of the RRAM device and the intrinsic mechanism were further investigated, revealing that the modulation of oxygen vacancies significantly affects the formation and rupture of CFs. This work presents a significantly simplified approach for WO_x-based RRAM. Unlike many systems that rely on complex doping, interface engineering, or heterostructures, we achieve stable digital switching merely by altering the top electrode material. This method effectively modulates oxygen vacancy distribution and conducting filament formation, offering excellent CMOS compatibility, superior device-to-device uniformity, and enhanced cycling stability. The experimental research provides valuable insights into the potential of WO_x-based resistive memories for practical data storage applications.

Supplementary material

See the supplementary material for the EDS spectra of the WO_x layer and additional details on other devices (Al/WO_x/Pt, Ti/WO_x/Pt and TiN/WO_x/Pt), including the *I*–*V* characteristics, the set/reset voltage distribution, the retention time, the fast pulse response, the *I*–*V* cycling characteristics and the pulse cycling characteristics.

Acknowledgements

This work was supported by the National Key Research and Development Program of China (Grant Nos. 2024YFA1611100 and 2023YFA1406500), the National Natural Science Foundation of China (Grant No. 12474099), and the Excellent Youth Project of Natural Science Foundation of Anhui Province (Grant No. 2308085Y07).

References

[1] Xia Q and Yang J J 2019 *Nat. Mater.* **18** 309
[2] Cheng C, Tiw P J, Cai Y, Yan X, Yang Y and Huang R 2021 *Sci. China Inform. Sci.* **64** 221402
[3] Messeri L and Crockett M J 2024 *Nature* **627** 49
[4] Mistry H K, Mavani C, Goswami A and Patel R 2024 *Educ. Admin. Theory Pract.* **30** 813
[5] Shen Z J, Zhao C, Qi Y F, Xu W Y, Liu Y N, Mitrovic I Z, Yang L and Zhao C Z 2020 *Nanomaterials* **10** 1437
[6] Rejeb A, Rejeb K, Appolloni A, Jagtap S, Iranmanesh M, Alghamdi S, Alhasawi Y and Kayikci Y 2024 *Internet Things Cyber-Phys. Syst.* **4** 1
[7] Zahoor F, Zulkifli T Z A and Khanday F A 2020 *Nanoscale Res. Lett.* **15** 90
[8] Dastgeer G, Nisar S, Rasheed A, Akbar K, Chavan V D, Kim D, Wabaidur S M, Zulfiqar M W and Eom J 2024 *Nano Energy* **119** 109106
[9] Kim J, Im J, Shin W, Lee S, Oh S, Kwon D, Jung G, Choi W Y and Lee J H 2024 *Adv. Sci.* **11** 2308460
[10] Xu X X, Luo Q, Gong T C, Lv H B, Liu Q and Liu M 2021 *Chin. Phys. B* **30** 058702
[11] Jung S, Park J, Kim J, Song W, Jo J, Park H, Kong M, Kang S, Sheeraz M, Kim I W, Kim T H and Park K 2021 *Npj 2D Mater. Appl.* **5** 90
[12] Oh H, Xiang Y, Redondo F G, Gupta M K, Perumkunnil M, Bardon M G, Dhiman A, Gowda S N, Walke A, Fantini A, Yasin F, Kar G S, Hellings G and Dehaene W 2024 *IEEE T. Electron Dev.* **71** 5380
[13] Yang Q, Han D, Zhao S, Kang J, Wang F, Lee S C, Lei J, Lee K J, Park B G and Yang H 2024 *Nat. Commun.* **15** 1814
[14] Chen J, Yu P, Zhao L, Li Y, Yang M, Xu J, Gao J, Liu W, Li J, Wang W, Kang J, Bu W, Zheng K, Yang B, Yue L, Zuo C, Cui Y and Luo J 2023 *Chin. Phys. B* **32** 027504
[15] Aryana K, Gaskins J T, Nag J, Stewart D A, Bai Z Q, Mukhopadhyay S, Read J C, Olson D H, Hoglund E R, Howe J M, Giri A, Grobis M K and Hopkins P E 2021 *Nat. Commun.* **12** 774
[16] Wintersteller S, Yarema O, Kumaar D, Schenk F M, Safonova O V, Abdala P M, Wood V and Yarema M 2024 *Nat. Commun.* **15** 1011
[17] Sun L, Zhang Y, Han G, Hwang G, Jiang J, Joo B, Watanabe K, Taniguchi T, Kim Y M, Yu W J, Kong B S, Zhao R and Yang H 2019 *Nat. Commun.* **10** 3161
[18] Ham W, Song Y W, Yoon J H, Lee S, Park J M, Lee J and Kwon J Y 2024 *Appl. Surf. Sci.* **670** 160595
[19] Bian J Y, Tao Y, Wang Z Q, Zhao X N, Lin Y, Xu H Y and Liu Y C 2024 *Chin. Phys. B* **33** 027301
[20] Fu L, Pan G, Hao R, Fan X and Li Y 2025 *Chin. Phys. B* **34** 077201
[21] Park J, Kumar A, Zhou Y, Oh S, Kim J H, Shi Y, Jain S, Hota G, Qiu E, Nagle A L, Schuller I K, Schuman C D, Cauwenberghs G and Kuzum D 2024 *Nat. Commun.* **15** 3492
[22] D'Agostino S, Moro F, Torchet T, Demirağ Y, Grenouillet L, Castellani N, Indiveri G, Vianello E and Payvand M 2024 *Nat. Commun.* **15** 3446
[23] Lu Y, Lee J H and Chen I W 2017 *Nanoscale* **9** 12690
[24] Hsu C C, Long P X and Lin Y S 2021 *IEEE T. Electron Dev.* **68** 95
[25] Sawa A 2008 *Mater. Today* **11** 28
[26] Zhu Y Y, Chen M Y, Lu H B, Mi P T, Luo D B, Wang Y Q, Liu Y, Xiong R and Wang H J 2024 *Appl. Phys. Lett.* **124** 063504
[27] Menke T, Dittmann R, Meuffels P, Szot K and Waser R 2009 *J. Appl. Phys.* **106** 114507
[28] Biju K P, Liu X J, Siddik M, Kim S, Shin J, Kim I, Ignatiev A and Hwang H 2011 *J. Appl. Phys.* **110** 064505
[29] Scott J C and Bozano L D 2007 *Adv. Mater.* **19** 1452
[30] Noman M, Sharma A A, Lu Y M, Kamaladasa R, Skowronski M, Salvador P A and Bain J A 2014 *Appl. Phys. Lett.* **104** 113510
[31] Zhou X, Gu D, Li Y, Qin H, Jiang Y and Xu J 2019 *Nanoscale* **11** 22070
[32] Nandi S K, Liu X J, Venkatachalam D K and Elliman R G 2015 *Phys. Rev. Appl.* **4** 064010
[33] Jeon H, Park J, Jang W, Kim H, Kang C, Song H, Seo H and Jeon H 2014 *Appl. Phys. Lett.* **104** 151603
[34] Yun H J, Ryu S Y, Lee H Y, Park W Y, Kim S G and Choi B J 2021 *Ceram. Int.* **47** 16597
[35] Kim G, Cho Y and Kim S 2024 *Chin. J. Phys.* **88** 1044
[36] Jafarpour S, Naghshara H and Parhizkar M 2024 *Mater. Chem. Phys.* **313** 128637
[37] Yadav P V K, Reddy Y A K, Ajitha B and Minnam Reddy V R 2020 *J. Alloys Compd.* **816** 152565

CPB Online In Press

[38] Zhang Z, Mo H, Li R, Zhou X, Lin Z, Zhang J, Tang X, Zhan Y and Luo J 2024 *Small Sci.* **4** 2300219
[39] Prakash A, Jana D, Samanta S and Maikap S 2013 *Nanoscale Res. Lett.* **8** 527
[40] Huang R M, Yan X Z, Ye S, Kashtiban R, Beanland R, Morgan K A, Charlton M D B and de Groot C H 2017 *Nanoscale Res. Lett.* **12** 384
[41] Abbas Y, Jeon Y R, Sokolov A S, Kim S, Ku B and Choi C 2018 *Sci. Rep.* **8** 1228
[42] Qi J, Huang J, Paul D, Ren J, Chu S and Liu J 2013 *Nanoscale* **5** 2651
[43] Jabeen S, Ismail M, Rana A M and Ahmed E 2017 *Mater. Res. Express* **4** 056401
[44] Won S, Lee S Y, Park J and Seo H 2017 *Sci. Rep.* **7** 10186
[45] Park J, Park E, Kim S G, Jin D G and Yu H Y 2021 *ACS Appl. Electron. Mater.* **3** 5584
[46] Waser R, Dittmann R, Staikov G and Szot K 2009 *Adv. Mater.* **21** 2632
[47] Zhang K, Ren Y, Ganesh P and Cao Y 2022 *Npj Comput. Mater.* **8** 76
[48] Zhang P, Ang Y S, Garner A L, Valfells Á, Luginsland J W and Ang L K 2021 *J. Appl. Phys.* **129** 100902
[49] Zhang P, Wang L, Ang K W and Fong X 2020 *Appl. Phys. Lett.* **117** 223101
[50] Lin C C, Tu B C, Lin C C, Lin C H and Tseng T Y 2006 *IEEE Electron Device Lett.* **27** 725
[51] Wu M C, Ting Y H, Chen J Y and Wu W W 2019 *Adv. Sci.* **6** 1902363

CPB Online In-Press